Electrochimica Acta 149 (2014) 1–10

Contents lists available at ScienceDirect

Electrochimica Acta

journal homepage: www.elsevier.com/locate/electacta

Analysis of the Deposit Layer from Electrolyte Side Reaction on the Anode of the Pouch Type Lithium Ion Polymer Batteries: The Effect of State of Charge and Charge Rate

Victor A. Agubra [a,*], Jeffrey W. Fergus [a], Rujian Fu [b], Song-yul Choe [b]

[a] Materials Research and Education Center, 275 Wilmore Laboratories, Auburn University, Auburn, AL 36849, USA
[b] Department of Mechanical Engineering, 1418 Wiggins Auburn University, Auburn, AL 36849, USA

ARTICLE INFO

Article history:
Received 1 August 2014
Received in revised form 13 October 2014
Accepted 14 October 2014
Available online 18 October 2014

Keywords:
Lithium ion battery
X-ray diffraction
Electrochemical properties
Electrode/electrolyte interface

ABSTRACT

The formation of the solid electrolyte interface (SEI) layer on the surface of the anode electrode of a lithium ion battery prevents further electrolyte decomposition reaction. However, at certain battery operating conditions, the SEI breakdown leading to more electrolyte decomposition reactions that form several species on the anode electrode surface. This paper focuses on the effect of battery potential and charge rate on the decomposition side reaction on the anode electrode of a lithium ion polymer battery, as a result of the breakdown of the SEI layer. The results from this study indicate that raising the state of charge (SOC) increases the rate of the electrolyte decomposition side reaction that resulted in formation of a thick deposit layer at the electrolyte/electrolyte interface. This deposit layer contains lithium that can no longer participate in the reversible electrochemical reaction. In addition, at high cycling potential and charge rates the amount of lithium in the graphite after complete cell discharge increased due to the entrapment of lithium in the graphite. The amount of irreversible capacity loss for the batteries cycled at high potential and current correlates with the amount of trapped lithium in the graphite and the growth of the deposit layer thickness at the electrode/electrolyte interface.

1. Introduction

The high energy/power density and excellent cycle life of the lithium-ion battery (LIB) compared to other batteries chemistries, e.g. lead acid and nickel-cadmium, have positioned it as the preferred portable energy source for most consumer appliances and in the automotive industry for electric vehicles (EV) and hybrid electric vehicles (HEV). However, several reported battery failures during its operation have raised several safety concerns for the LIBs, thus hampering its large scale application. The performance of the lithium-ion battery depends on the development of materials for the various battery components [1–3]. The degradation of these components during operation adversely affects the energy delivery of the LIB. Mechanisms such as loss of accessible lithium ions, degradation of electrodes, binder, current collectors, and decomposition of the electrolyte have been reported to contribute to battery capacity fade [4–7].

A robust SEI layer will prevent further electrolyte solvent reduction on the carbon electrode. However, at elevated temperature, the metastable species $ROCO_2Li$ within the SEI layer decomposes into more stable compounds $-Li_2CO_3$ and LiF, which distort the SEI layer and create a porous SEI structure that exposes the graphite surface to more electrolyte decomposition reaction [8,9]. The distortion of the SEI layer leads to the formation of additional deposit layers on top of the SEI. These side reactions tend to consume recyclable lithium ions [9]. In addition, the surface layer formed on the anode could clog the pores on the carbon anode electrode and may limit the accessibility of lithium ions to the anode surface [10,11], which can lead to an increased in the charge transfer/Ohmic resistance and overall impedance of the battery [12–15]. This surface layer affects the electrochemical reaction on the surface of the anode and thus impacts on the reversible capacity of the LIB.

This paper presents a quantitative and qualitative analysis of the effect of the state of charge (SOC) and charge rate on the growth of the deposit layer at the anode electrode/electrolyte interface. In this work the deposition due to solvent reduction was observed only at the graphite electrode - reaction on the cathode was considered negligible. Understanding how the battery charging protocol influences the formation of the deposit layer is critical to effectively controlling/limiting these operational parameters to extend the operational lifetime of the lithium ion battery.

* Corresponding author. Tel.: +13348443353, fax: +13348443400.
E-mail address: aa0002@auburn.edu (R. Fu).

http://dx.doi.org/10.1016/j.electacta.2014.10.076
0013-4686/

2. Experimental

2.1. Battery Chemistry

The batteries used in this study were large format pouch type-lithium ion polymer batteries from battery manufacturer LGChem with a $Li(Mn,Ni,Co)O_2$ cathode and the anode material made of carbon with polyvinylidene fluoride (PVDF) as the binding material. The current collectors of the anode and cathode electrodes are copper and aluminum, respectively. The electrolyte is an inorganic salt, $LiPF_6$, with co-solvents of ethylene carbonate (EC), and dimethyl carbonate (DMC). The nominal capacity of each battery is 15.7 Ah with an operating voltage level of 2.5 to 4.15 V.

2.2. Cycling Test

The charge/discharge cycles were performed using an in-house designed test station comprised of a programmable charging system, a programmable electronic load system and a data acquisition system that are computer controlled using LabVIEW™. The testing system allowed for the input of various charging conditions, such as C-rate and state of charge (SOC). The battery fixture was located in an environmental chamber to allow for control of the external temperature at 25 °C ± 2 °C.

The batteries were charged by a constant current-constant voltage (CC-CV) charging protocol at room temperature (25 °C ± 2 °C). In each cycle, the batteries were discharged with a constant current until the terminal voltage decreased to the voltage corresponding to the desired lower SOC (e.g. 25% = 3.13 V) and then charged with a constant current up to the voltage corresponding to the upper SOC (e.g. 3.78 V) followed by a constant voltage (CV) charge. After every 20 cycles, a 1 C (15.7 A) discharge-resting-charge profile was applied to the battery to measure its capacity. The capacity (Q_{max}) was calculated by integrating the current when the cell is being discharged from 100% to 0% SOC (i.e. 4.15 V to 2.5 V) using 1 C current (15.7 A) at room temperature. The Q_{max} data for each battery was recorded every 20 cycles. The battery was rested for 10 minutes before and after the Q_{max} measurement. The pre-test terminal voltages for the desired SOC were determined by coulomb counting and then adjusted by capacity. Table 1 summarizes the test matrix used in cycling the batteries.

Table 1
Test matrix used to carry out the electrochemical aging experiment, each battery was cycled at SOCs set within 65% capacity band of the battery.

State of Charge	Equivalent cycling Voltage (V)	C-rate/Current (A)	Other Conditions
25–90%	3.13–3.78	4C/62.8	25 °C @ 600 cycles
5–70%	2.63–2.94		
25–90%	3.13–3.78	3C/47.1	
5–70%	2.63–2.94		
25–90%	3.13–3.78	2C/31.4	
5–70%	2.63–2.94		

2.3. Electrochemical impedance spectroscopy (EIS)

A Gamry electrochemical impedance spectroscopy (EIS) framework in galvanostatic mode was used to apply different frequencies (1 mHz to 1 kHz) of small AC excitation current (1 A) to battery and voltage responses were collected at 25 °C. A bipolar power supply was used to amplify the signal from EIS signal board. The measured impedances of the batteries were fit using the equivalent circuit model (Fig. 3a insert) was used to extract resistances, the SEI

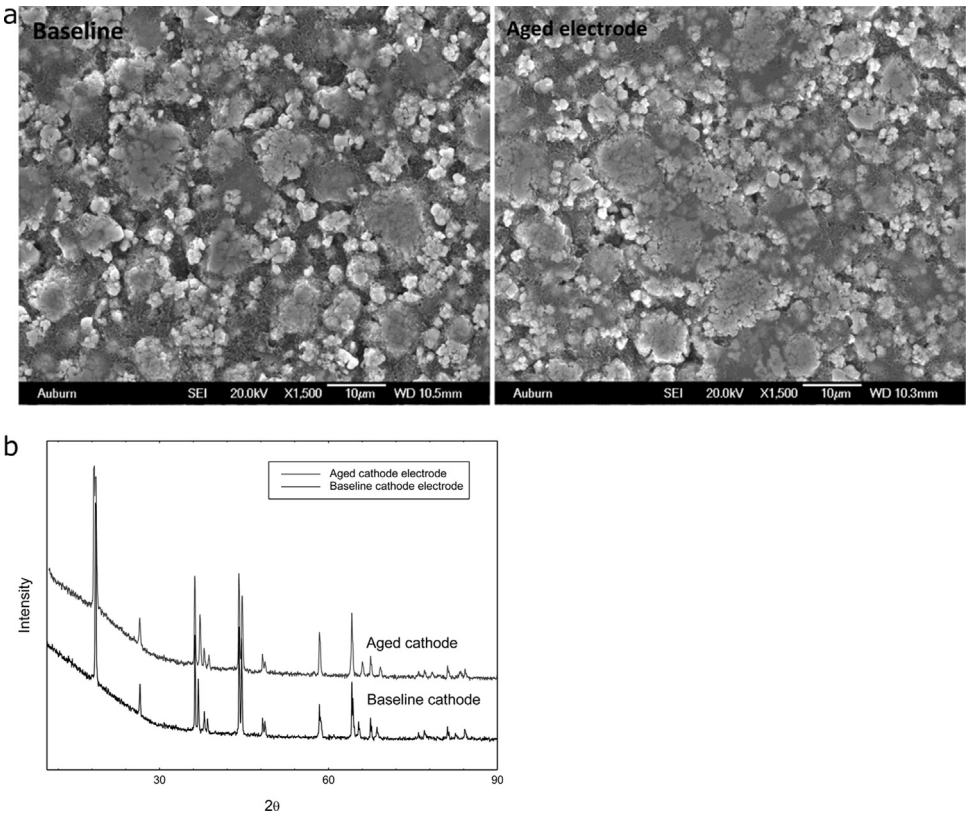

Fig. 1. (a) SEM micrograph showing the similarity of surface morphology of the baseline cathode and aged cathode electrode after cycling 600 cycle at 25–90% SCO and 4 C charge rate, (b) XRD spectra of baseline and aged cathode electrode showing no new phases formed aged aging the cell at 25–90% SOC and 4 C charge rate.

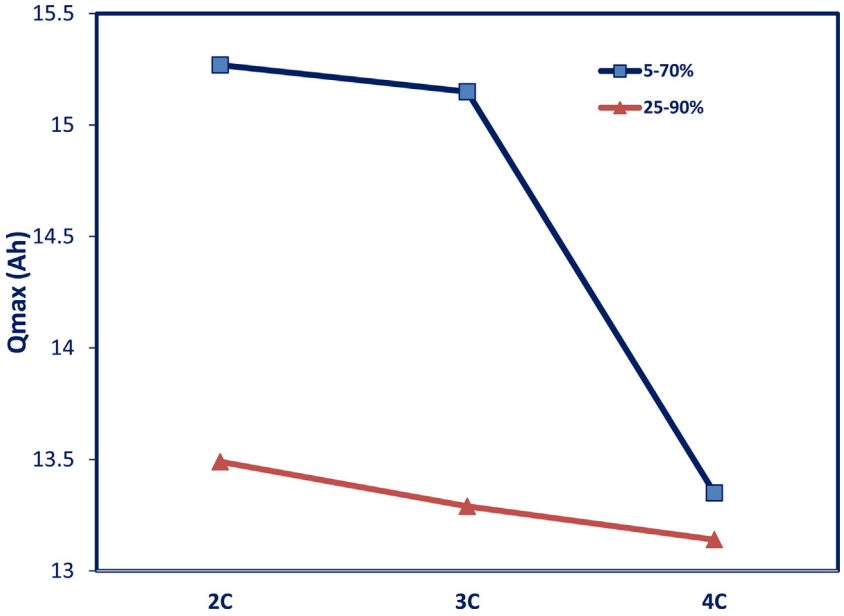

Fig. 2. comparison of capacity fade for cells aged at 25–90% SOC and 5–70% SOC as a function for the charge rate.

film resistance(R_{sei}), the Ohmic resistance(R_0), and the charge transfer resistance(R_c), by fitting the EIS-ECM impedance spectrum using a complex algorithm [16].

2.4. Materials Postmortem Analysis

After cycling and measurement of the capacity and impedance, the batteries were discharged to 0% SOC (2.5 V) and dismantled in an argon atmosphere in glove box. The harvested electrode were cleaned in DMC and dried in a desiccator inside the glove box. Cleaning the anode with dimethyl carbonate solvent was to remove any excess organic compounds from the electrode surface. The cleaning process did not significantly impacted on the both the SEI and deposit layer. The microstructure and surface morphology of the cathode electrode showed no deposition after aging (Fig. 1), therefore the deposition due to solvent reduction reaction on the cathode/electrode interface was considered negligible. The anode electrode, however, showed deposition of side reaction products on the carbon particle surface. The quantitation of the thickness of the formed deposit layer was carried out by taking a cross sectional view (the samples were mounted on an epoxy and the edges polished) of the deposited surface layer and measuring its thickness using a scanning electron microscope (SEM). A total of eight electrodes were selected from each battery to represent the range of the amount of deposit. Specifically four electrodes with large amounts of deposit and the other four with small to medium amounts of deposits by physical examination. For each of electrode eight (8) samples, six different deposit thickness were measured. Therefore for each battery, the thickness of the deposited layer was calculated by taking the mean value of the 48 measured thicknesses.

The graphite crystal lattice parameters and the formation of possible new phases were investigated using the Bruker D8 X-ray diffraction (XRD). The EVA and PDFmaint software were used to analyze and index the peaks pattern for the aged and baseline (fresh cell) anode electrode. The composition of the surface film was also analyzed using Fourier transformed infra-red spectroscopy (FTIR) and X-ray photoelectron spectroscopy (XPS). For FTIR analysis, Bruker optics equipped with single-reflection attenuated total reflection (ATR) accessory was used. The electrode samples were adjusted such that the beam was directly on the deposit layer area to ensure maximum absorbance. Each spectrum was recorded

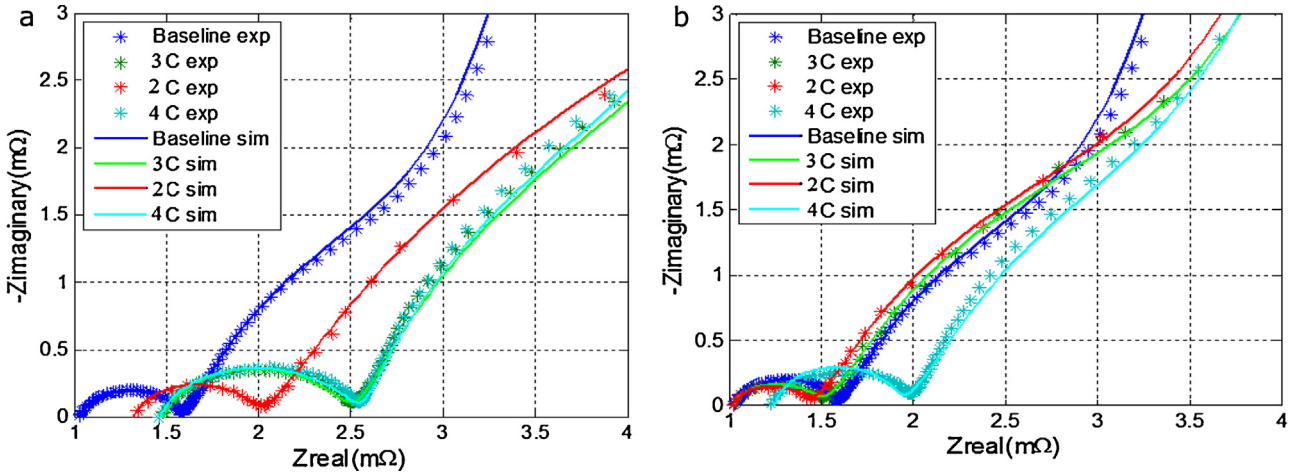

Fig. 3. (a) Impedance with fit from model for the cell at 25–90% SOC as a function of charge rate, (b) Impedance with fit from model at different charge rate for the 5–70% SOC.

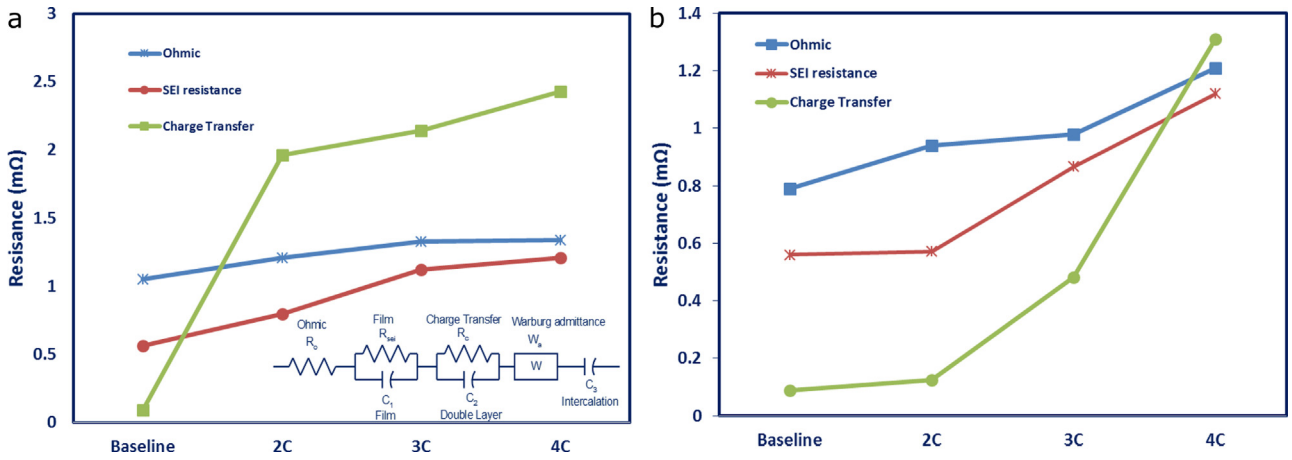

Fig. 4. (a) Extracted resistance from equivalent circuit model for cell aged at 25–90% SOC at different charge rate, (b) Extracted resistance from equivalent circuit model for cell aged at 5–70% SOC at different charge rate.

by accumulating 128 scans with a resolution of 4 cm. For XPS analysis, a VG ESCA scientific theta probe spectrometer was used. Samples were prepared according to XPS sample standard (1 mm × 1 mm) and transferred to the XPS spectrometer inside an argon-filled sample box. The carbon 1 s peak at 285 eV was used as the binding energy scale reference, and the Ag 3d5/2 line at 368 eV with full width at half maximum (FWHM) of 0.66 eV was used to calibrate the spectrometer. To achieve high-resolution spectra, a constant pass energy of 50 eV was used and the pressure in the analysis chamber was maintained at 6×10^{9} mbar. Data analyses were performed using Gaussiane Lorentzian curve fitting with Shirley background subtraction.

3. Result and Discussion

3.1. Capacity fade of aged batteries

The capacity fade for the batteries cycled at the two SOC levels are shown in Fig. 2. The Q_{max} results indicate that reducing the charge rate while cycling the batteries at high SOC did not significantly reduce the irreversible capacity of the cell. At 4 C, the capacity fade was 17.8% compared to 15.7% at 2 C. At lower potential (i.e. 5–70% SOC) however, the charge rate significantly impacted the capacity retention of the batteries. At low C-rate (2. C), the cell's capacity was comparable to the baseline cell (15.7Ah) with a 4.6% loss, but the capacity loss increased sharply as the charge rate was increased to 4 C. A similar trend in the battery impedances for the two SOCs was observed as shown in Fig.3a and Fig. 3b. For instance, the impedances of the batteries cycles at 25–90% SOC increased progressively as the charge rate was increased from 2 C to 4 C. On the contrary, the impedances of the batteries cycled at 5–70% SOC was relatively unchanged between 2 C and 3 C charging rates, but increased significantly for a 4 C charging rate, which is consistent with the results from the capacity fade. Lithium plating which manifest as a voltage overshoot (over potential) at cell discharge, due to a much lower potential than that of lithium de-intercalation potential created at the anode electrode[17], was absent, which implied that did not occur at high SOC and charge current. Therefore the contribution of plated lithium on the batteries capacity fade was assumed insignificant. The extracted resistance from the equalvalent circuit model: Ohmic, SEI, and charge transfer resistance for the two SOCs plotted in Fig. 4a and 4b show a progressive increase in all the resistances. The charge transfer resistance, in particular, had the highest increase as the charging current was increased. A comparison of the charge transfer resistance for 25–90% SOC and that for 5–70% SOC (Fig. 5) with different charge rates showed that at high SOC the charge transfer resistance changed little with increasing charge rate, but for low SOC (5–70%) increased sharply as the charge rate increased from 3 C to 4 C. The explanation for these observed increases in the charge transfer resistance became apparent from the materials characterization of the deposit layer at the electrode/electroyte interface and the structural analysis of the aged anode electrode.

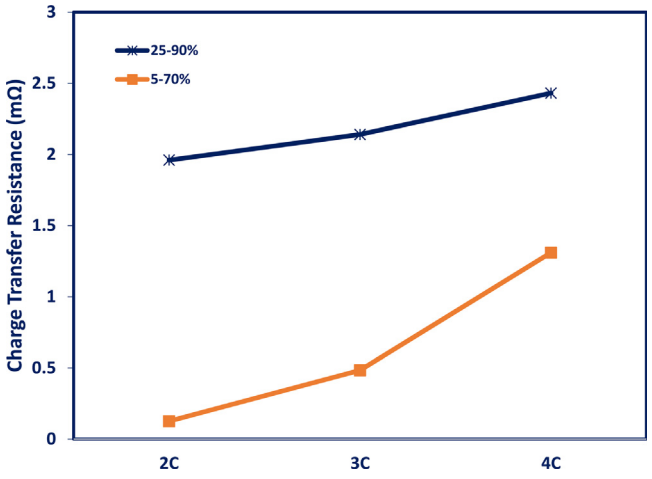

Fig. 5. Comparison of the charge transfer resistance as a function for the charge rate for the 25–90% and 5–70% SOC range.

3.2. Surface deposit layer growth characterization

The side reaction on the anode/electrolyte interface produced reaction deposits on the surface of the electrode as shown in Fig. 6a and Fig. 6b. For the cells cycled at 25–90% SOC, large agglomerates of deposits on the electrode were similar for charging at 4 C and 3 C, while the deposit layers were isolated agglomerates when the charge rate was reduced to 2 C. In the case of the low potential, cycling at 4 C produced deposit agglomerations similar to those observed for 25–90% SOC charging at 3 C. As the charging current was reduced to 2 C for the 5–70% SOC, the deposits were not obvious on the surface of the anode electrode at low magnification. At high magnification, the deposits on the carbon particles were thin, with its thickness estimated to be between 100 nm–1 μm.

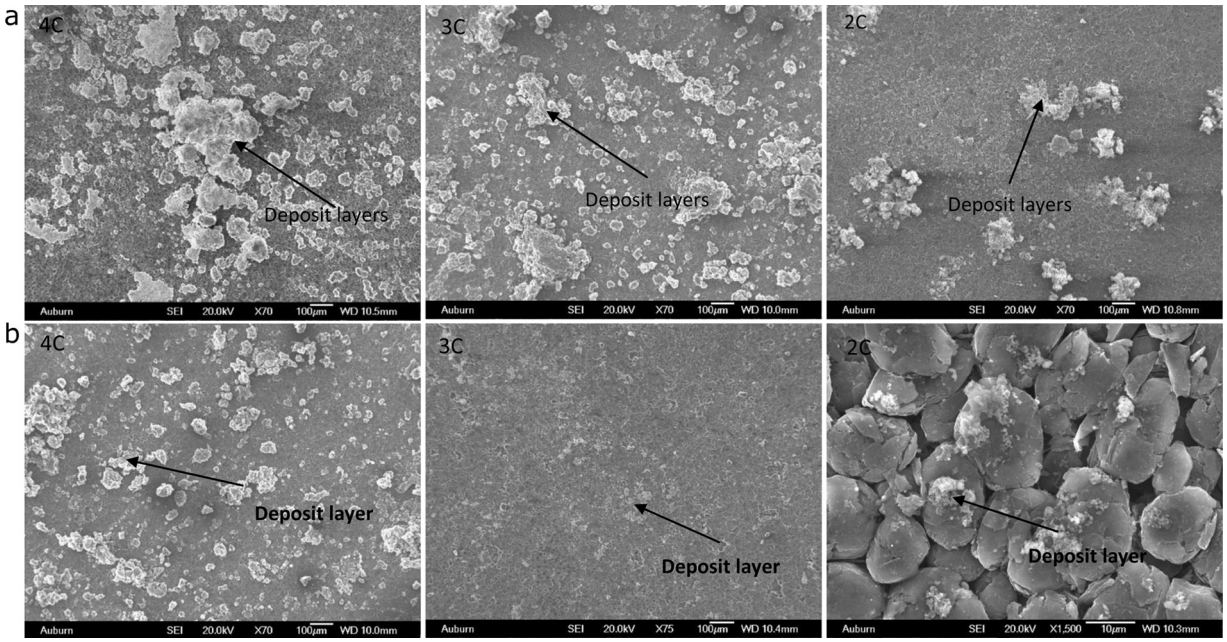

Fig. 6. (a) Surface distribution of deposit layer at different charge rate for cell aged at 25–90% SOC, (b) Distribution of the deposit layers on the electrode surface for the cell aged at 5–70% SOC at different charge rate.

$$\rightarrow = i_a = nFk_{red}C_{red}\exp\left(\frac{\alpha\Phi}{RT}\Phi\right)$$
$$i$$

A high battery potential during charging creates a region of high polarization on the surface of the anode electrode (overpotential). At this region of high polarization, the current density of the anode is governed by a kinetic like Butler equation;

where i_a is electrolyte reduction current density, C_{red}, is the electrolyte concentration, Φ, is the electrode potential, and β is the charge transfer coefficient. Therefore the reaction rate occurring on the electrode surface becomes a function of the migration or electrolyte concentration and the electrode potential. A high battery potential during charging will thus create a region of high polarization, thereby creating a situation where different parts of the electrode surface could reach different Li deposition potentials. Therefore cycling the battery at this high charge rate coupled with a high potential accelerated the passivation reaction. At these operating conditions, the solid electrolyte interphase (SEI) layer became thicker at the aged electrode compared to that formed on the baseline (Fig. 7) thus rendering the SEI layer ineffective [18]. The ineffectiveness of the SEI layer as a protective layer on the carbon particles thus allowed further electrolyte decomposition reactions to occur, thus producing larger non-uniform deposit layers.

The thicknesses of these deposits layers for different charge rates, as shown in Fig. 8a and Fig. 8b (with the exception of 2 C at the 5–70% SOC) at the two different SOCs are plotted in Fig. 9. This showed a linear relationship between the charge rate and the deposit layer growth. In reducing the charge rate, there was a comparable reduction in the deposit thickness for the two different SOCs. Cycling the cell at high SOC produced a considerable amount deposit thickness (37 μm) even at low charge rate of 2 C. While lowering the SOC (5–70%) and the charge rate to 2 C produced a thinner deposit layer of less than 1 μm thick. These deposits on the surface of the anode electrode could block diffusion into the porous anode electrode and contribute to the high interfacial resistance at the electrode/electrolyte interface. The increase in charge transfer resistance along with the Ohmic and the SEI resistances for the two

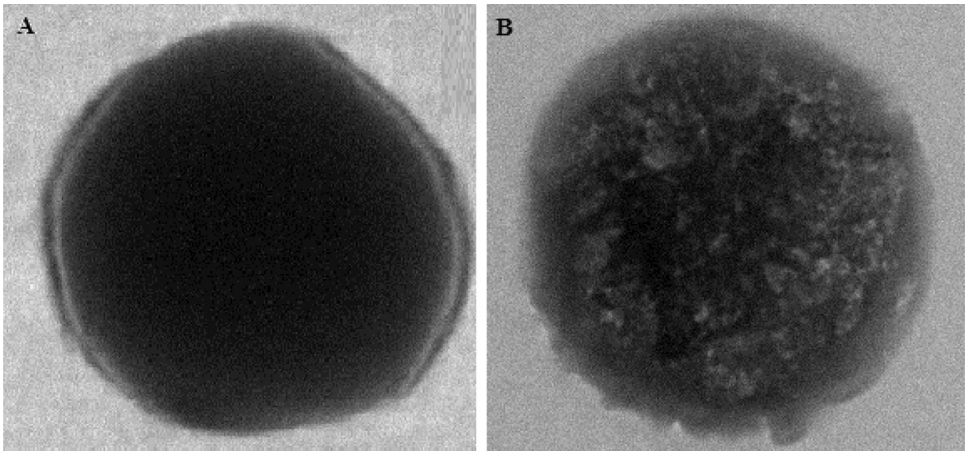

Fig. 7. TEM micrographs showing the growing SEI layer for a cell cycled at (b) high SOC and high charge rate and (a) that formed on the baseline carbon particles.

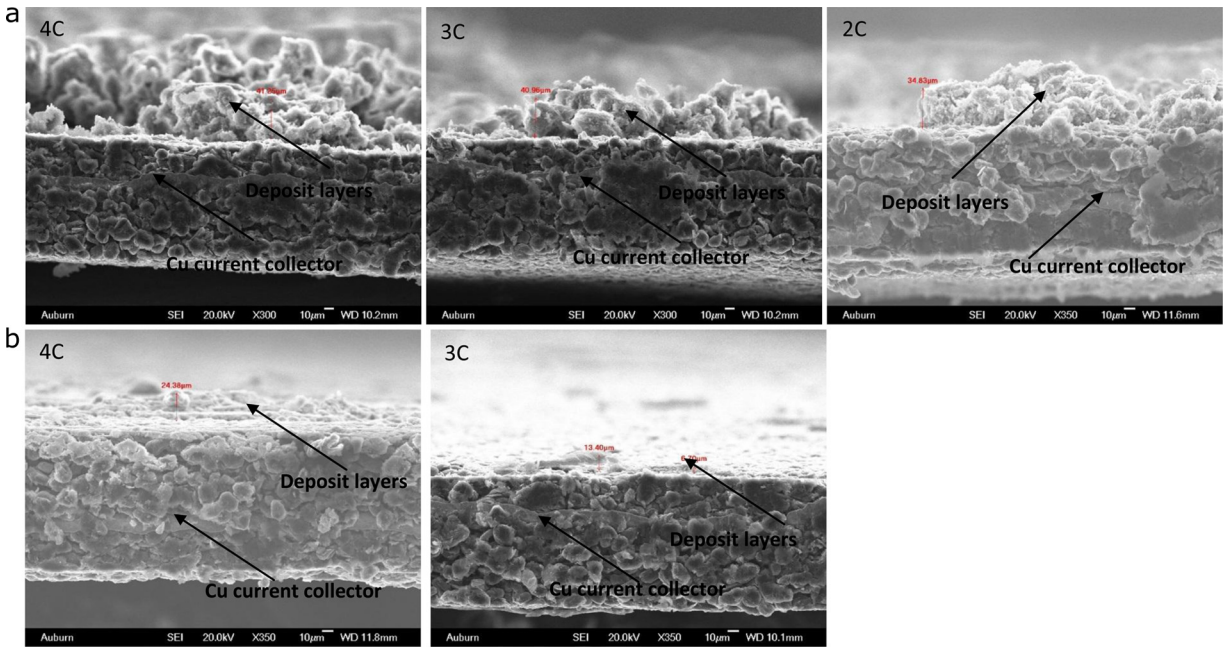

Fig. 8. (a) Cross sectional view of deposit layer on anode surface for different charge rate, (b) Cross sectional view of the deposit layer at different C-rate for the aged cell at 5–70% SOC.

SOCs regimes, as the charge rate was increased correlated with the growth of the deposit layer thickness at the electrode/electrolyte interface.

3.2.1. Deposit layer composition analysis: FTIR analysis

The FTIR spectra, shown in Fig. 10, contain bands at 1750 cm^{-1} that represent the stretching vibration of C=O in EC (alkyl carbonate), and absorption bands at 1300 cm^{-1} and 1450 cm^{-1} that represent asymmetric stretching vibration of the C-O-C and CH_2 bending vibration of decomposition products of the electrolyte solution, respectively [19]. The main chemical constituents of the SEI layer in $LiPF_6$–EC/DMC solutions are $ROCO_2Li$ and Li_2CO_3 [20], which generally have spectra at 1600 cm^{-1} and 1300 cm^{-1} for $ROCO_2Li$ and 860 cm^{-1} and 1375 cm^{-1} for Li_2CO_3. The FTIR analysis indicates that the chemical constituents of the deposit layer are the same as those constituting the SEI layer.

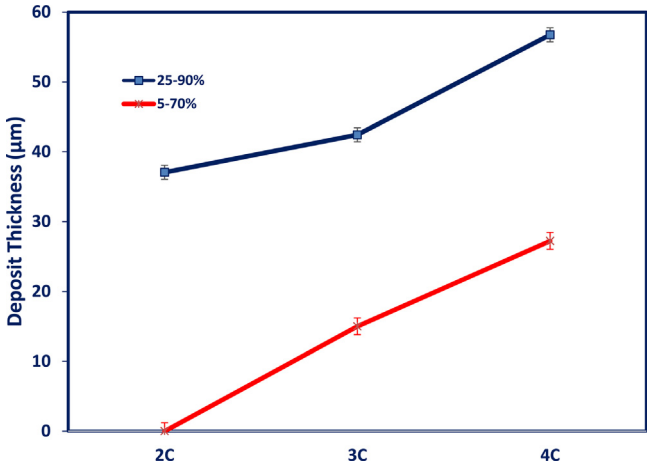

Fig. 9. A comparison of deposit layer thickness s at the different charge rate for the 25–90% SOC aged cell.

3.2.2. Deposit layer composition analysis: X-ray photoelectron spectroscopy

The baseline XPS spectrum for the carbon anode clearly shows a graphite peak at range of 284.3– 284.8 eV (Fig. 11a). A small peak in the 290–291 eV range corresponds to the C-F bond in the PVDF binder materials. The peak at 533 eV was the most prominent peak in the O1s spectra for the aged anode electrode (Fig. 11b). Furthermore, Li_2CO_3 (expected at 531.5 eV), and species like Li_2O and LiOH (expected <530 eV) were detected in the O1s spectra. An increase in the peak of the Li 1 s at 55.1 eV for the aged electrode was consistent with the existence of LiF species on the deposit layer. The electrolyte contains impurities such as H_2O and oxygen, which can lead to the formation of LiOH and Li_2O. The lithium amount in the baseline and the aged battery were similar as shown in Table 2, The XPS signal is limited to 1–2 nm, so this composition represented the outer surface of the deposit layer.

3.3. Analyzing the lithium content trapped in the graphite

X-ray diffraction for the aged anode indicated a new phase with a peak at 2θ 64° (Fig. 12) in addition to those peaks patterns for the carbon and the copper current collector, which is attributed to LiF. The LiF species is reported to form a resistive layer on the anode electrode [21], which contributes to the observed increased in cell resistance. The (0 0 2) peak for graphite (Fig 13a and 13b) after aging shifted to lower 2θ angles and broadened, which was attributed to the presence of lithium in the graphite layers after the electrode was discharged to 2.5 V (0% SOC).

Table 2
XPS studies showing the elemental composition of the surface layer from the C1s, O1s and Li1s analysis of the aged anode electrode compared to those from the baseline anode electrode.

Condition	Li	C	O	F
Baseline cell	40	26	33	1
Aged cell	44	26	28	2

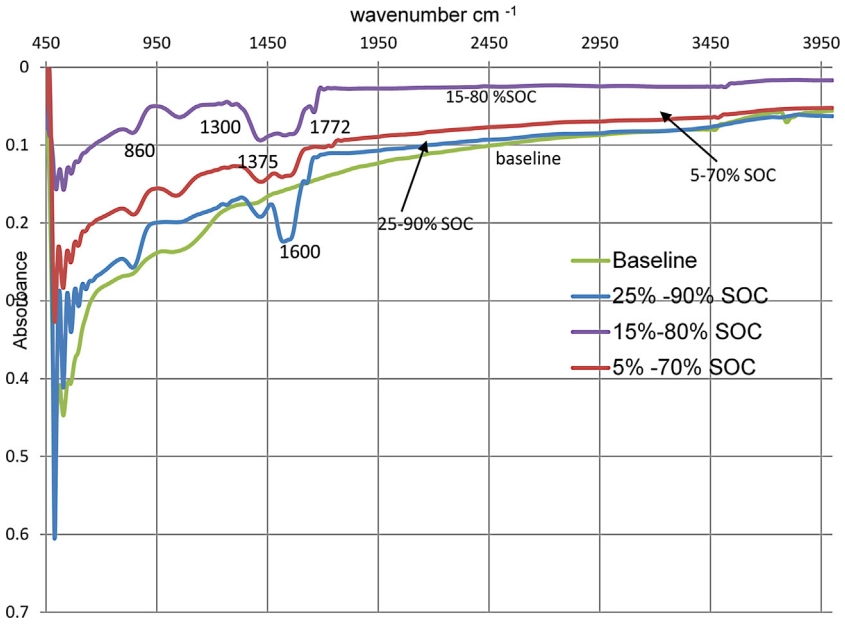

Fig. 10. FTIR analysis of the compounds constituting the deposit surface layer.

All the cells were discharged to 0% SOC (2.5 V), thus some amount of lithium would remain in the graphite structure because 0% SOC does not equal to 0% Li in the crystal structure of the graphite. The shifts of the (0 0 2) peak to lower 2θ° relative to the baseline, indicates that a larger concentration of lithium remained in the graphite structure after discharge. The (0 0 2) peak for both the baseline and the aged cell had a shoulder, which was deconvoluted into two separate peaks using the Lorenz area function (Fig. 13c). The range of d-spacings corresponds to a range in lithium content which indicates that some particles had higher lithium content while other had low lithium content in the graphite electrode matrix.

The analysis of the d_{002} for the high SOC showed that the lower d_{002} values were significantly above that of the upper d_{002} of the baseline within an uncertainty of ±0.0014 Å for batteries cycled at 3 C and 4 C charge rate (Fig. 14a). In addition, the upper d_{002} values for batteries cycled at both high and low potentials at charge rates 3 C and 4 C were significantly higher compared to the upper d_{002}

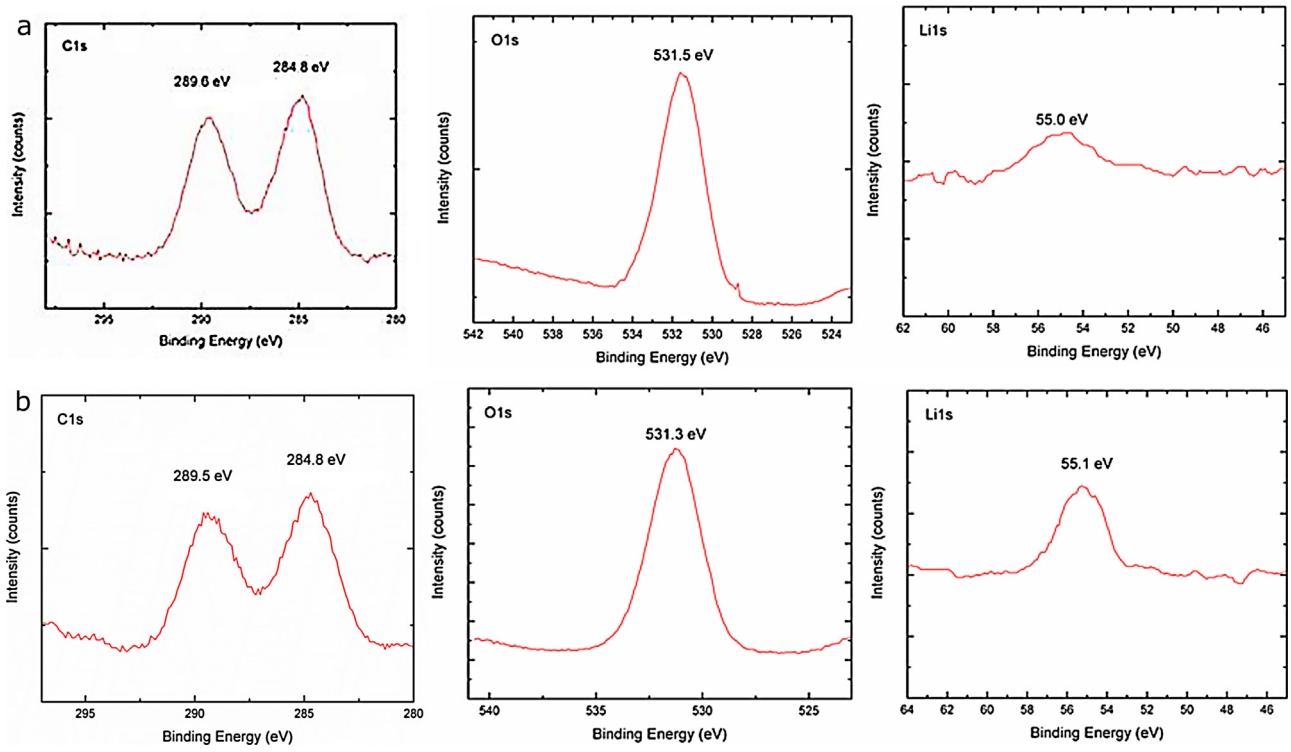

Fig. 11. (a) High resolution XPS spectra over the C1s, O1s, and Li1s portions regions from the baseline cell, (b) High resolution XPS spectra over the C1s, O1s, and Li1s portions regions from aged 25–90% SOC at 4 C cell.

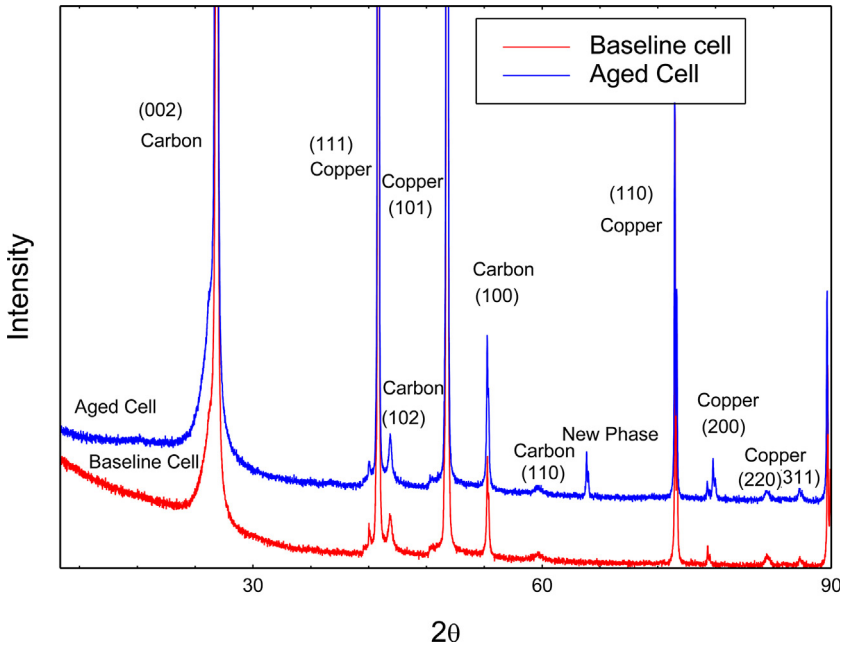

Fig. 12. X-rays diffraction spectra for aged and baseline for the anode electrode.

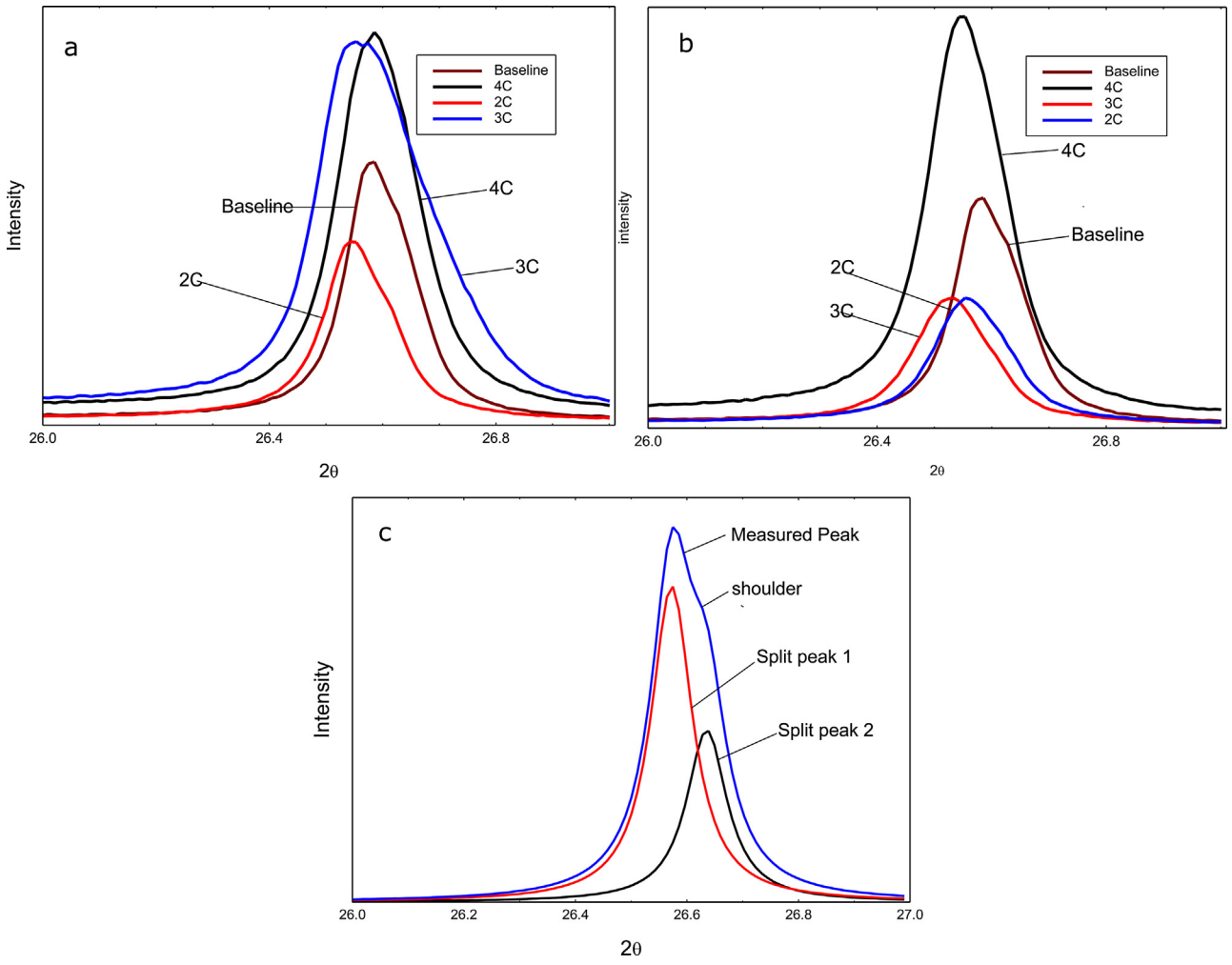

Fig. 13. (a) XRD spectra for the 0 0 2 peak for the 5–70% SOC at different charge rate, (b) XRD spectra for the 0 0 2 peak for the 25–90% SOC at different charge rate, (c) Deconvoluted peaks for the shoulder on the baseline (0 0 2) peak.

Table 3
Weighted average change in graphite lithium composition and the amount trapped in the graphite layers for aged anode electrode.

SOC	Charge rate	Weighted Average (X in Li_xC_6)	Lithium Trapped (%)
Baseline	-	0.21685	–
5–70%	4 C	0.23285	2.34
25–90%		0.27215	8.09
5–70%	3 C	0.23401	2.5
25–90%		0.26905	7.6
5–70%	2 C	0.22595	1.3
25–90%		0.23715	3.0

for the baseline graphite electrode. On the other hand, for batteries cycled at low current (2 C); for the low potential, both the upper and lower d_{002} values were statistically comparable to those of the baseline graphite electrode, while for the high potential regime both the lower and upper d_{002} values and were significantly higher than the corresponding upper and lower d_{002} values for the baseline.

The amount of trapped lithium in the graphite was estimated by calculating the difference between the x (Li_xC_6) in the discharged baseline cell and compared to the x (Li_xC_6) in the aged discharged cell from the weighted x values tabulated in Table 3. The increase in the lithium content in the graphite for the aged anode relative to the baseline was an indication that some of the lithium was "trapped" in the graphite after the discharge cycle. The trapping of the lithium in the graphite sheets at the end of discharge was attributed to the excessive polarization of the anode electrode. In the ideal case, the same level of lithium is expected to be in graphite for both the aged and the baseline electrode at the end of each discharged cycle. The amount of lithium trapped in the graphite tends to increase for the high SOCs at charging rates of 3 C and 4 C (Fig. 14b). This similarity in the amount of lithium trapped in the graphite sheets for the high SOC for the 4 C and 3 C correlates with their respective capacity fade (i.e. 17.9% and 16.9% capacity fade for 4 C and 3 C, respectively) as summarized in Table 4. However, as the charge rate was reduced to 2 C the amount of lithium trapped was reduced considerably. This, however, did not correlate with the loss in capacity at 2 C, which was about 15.7% at high SOC. This capacity loss was attributed to the thick deposit layer (37.1 μm) on the graphite particles.

For lower SOC, cycling the batteries at lower charge rates resulted in most of the lithium content within the graphite being reversed to the cathode during discharge, correlates well with the capacity fade results for the 2 C at 5–70% where the battery loss about 0.5Ah (4.1%). These trapped lithium ions were isolated from the electrochemical process, which contributed to the high capacity fade of the batteries observed at high SOC. Therefore, cycling the batteries at high SOC irrespective of the charge rate produced a significant surface deposit layer that contained a large amount of lithium, in addition to the trapped lithium within the graphite which did return to the cathode electrode during the discharge process, which was consistent with results from our physic based model [22].

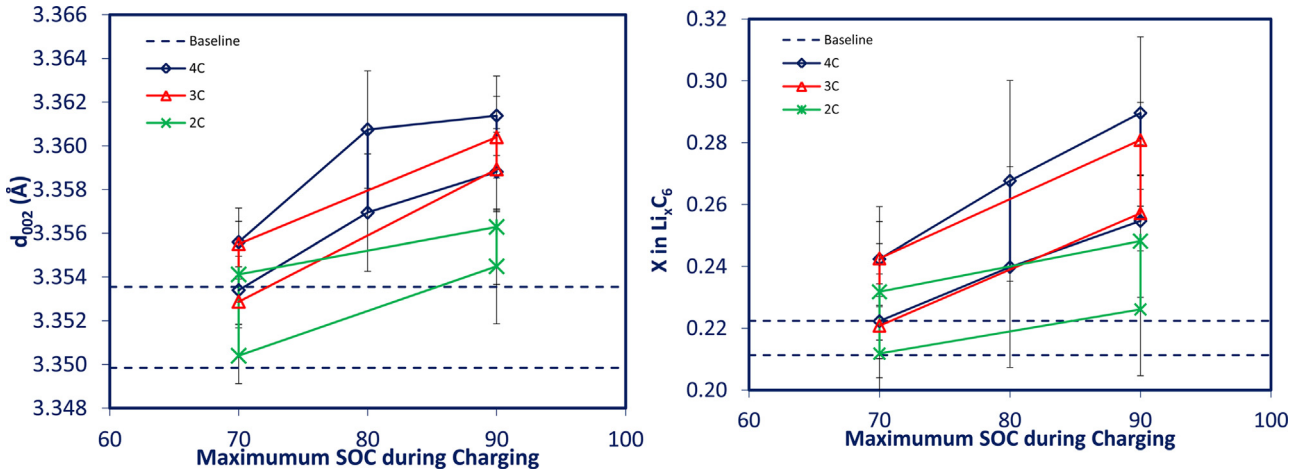

Fig. 14. (a) The d-spacing for the de-convoluted peaks as a function of SOC and charge rate, (b) Lithium content in the graphene layers as a function of SOC and charge rate.

Table 4
A summary of the correlation between the capacity loss, deposit layer thickness and the amount lithium trapped in graphite layers for the aged batteries anode electrodes.

State of Charge	Charging rate	Capacity Fade (%)	Deposit Layer thickness(μm)	Amount of Lithium Trapped (%)
25–90	4 C	17.8	56	8.1
5–70%		7.8	27	3.2
25–90	3 C	16.9	42	7.6
5–70%		5.3	15	2.5
25–90	2 C	15.7	37	3
5–70%		4.6	1	1.3

4. Conclusion

Results from this study showed that reducing the charge rate while cycling the batteries at high potential did not reduce the parasitic side reaction at the electrode/electrolyte interface. There was a significant thick deposit layer build-up on the electrode surface even when the charge rate was reduced to 2 C. A lower potential resulted in a lower deposit thickness as the charge rate was lowered. This deposit layer contained lithium that was not available for further electrochemical reaction. The high cycling potential and charge rate created a substantial amount of lithium trapped in the graphite which did not return to the cathode electrode during the discharge process. A direct correlation was established between the high irreversible capacity loss for the cells cycled at high potential and current and the amount of lithium trapped in the graphite and the growing deposit layer thickness at the electrode/electrode interface.

References

[1] M.S. Whittingham, MRS Bull 33 (4) (2008) 411–419.
[2] A. Patil, V. Patil, W.D. Shin, J.W. Choi, D.S. Paik, J. Yoon, Mater Res Bull 43 (2008) 1913–1942.
[3] A.K. Shukla, T.P. Kumar, Curr. Sci. 94 (2008) 314–331.
[4] M. Dolle, L. Sannier, B. Beaudion, M. Trentin, J. Electrochem. Soc. 5 (2002) A286.
[5] M. Wolfgang, C. Lu, P. Novak, J. Electrochem Soc. 158 (2011) A1478.
[6] N.N. Sinha, T.H. Marks, H.M. Dahn, A.J. Smith, J.C. Burn, D.J. Coyle, J.J. Dahn, J.R. Dahn, J. Electrochem. Soc. 159 (2012) A1672.
[7] A. Agubra, J. Fergus, J. Power sources 268 (2014) 153.
[8] W. Li, C. Campion, L.B. Lucht, B. Ravdel, J. Dicarlo, K.M. Abraham, J. Electrochem. Soc. 152 (2005) A1361.
[9] S. Lee, S.B. Pyun, Carbon 40 (2002) 2333.
[10] M.D. Levi, C. Wang, J.S. Gnanara, D. Aurbach, J. Power Sources 119 (2003) 538.
[11] J.P. Fellner, G.J. Loeber, S.S. Sandhu, J. Power Sources 81 (1999) 867–871.
[12] M.C. Smart, B.V. Ratnakumar, S. Surapudi, Y. Wang, X. Zhang, S.G. Greenbaum, A. Hightower, C.C. Ahn, B. Fultz, J. Electrochem. Soc. 46 (1999) A3963.
[13] P.L. Moss, G. Au, E.J. Plichta, P.J. Zheng, J. Electrochem. Soc. 157 (1) (2010) A1.
[14] G. Sarre, P. Balanchard, M. Broussely, J. Power Sources 127 (2004) 65–712.
[15] N.N. Sinha, A.J. Smith, J.C. Burns, J. Gaurav, K.W. Eberman, E. Scott, J.P. Gardner, J.R. Dahn, J. Electrochem. Soc. 158 (2011) A1194.
[16] R. Bhattacharyya, B. Key, H. Chen, A.S. Best, A.F. Hollenkamp, C.P. Grey, Nat Mater. 9 (2010) 504.
[17] B.V. Ratnakumar, M.C. Smart, J. Electrochem. Soc. Trans. 25 (2010) A241.
[18] Y. Domi, M. Ochida, S. Tsubouchi, H. Nakagawa, T. Yamanaka, T.T. Doi Abe, Z. Ogumi, J. Phys. Chem. C 115 (2011) 25484.
[19] C. Huang, S. Zhuang, F. Tu, J. Electrochem Soc. 160 (2013) A37.
[20] S.I. Pyun, Y.G. Ryu, J. Electroanal. Chem. 455 (1998) 11.
[21] L. Yang, T. Markmaitree, B.L. Lucht, J. Power Sources 196 (2011) 2251.
[22] R. Fu, S.Y. Choe, V. Agubra, J. Fergus, J. Power source 261 (2014) 120.